

pubs.acs.org/journal/apchd5 Article

Plasmon Launching and Scattering by Silicon Nanoparticles

Artyom Assadillayev, Tatsuki Hinamoto, Minoru Fujii, Hiroshi Sugimoto, Mark L. Brongersma, and Søren Raza*



Cite This: ACS Photonics 2021, 8, 1582-1591



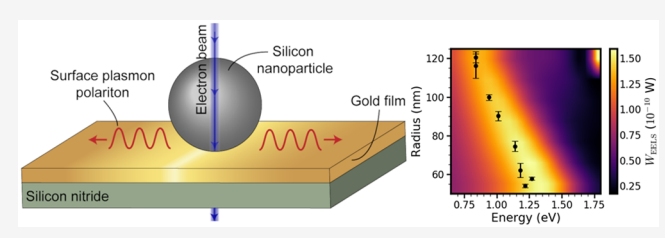
ACCESS

Metrics & More

Article Recommendations

SI Supporting Information

ABSTRACT: Resonant optical nanomaterials with a high refractive index, such as silicon, have become key elements for controlling free-space light. Here, we show that silicon nanoparticles can manipulate highly confined guided waves in the form of surface plasmon polaritons (SPPs) on a subwavelength scale. Using electron energy-loss spectroscopy in a transmission electron microscope, we demonstrate that SPPs in ultrathin metal films can be efficiently launched due to the strong coupling between the Mie



resonances of the nanoparticle and the SPP modes. We find that the SPP excitation wavelength can be tuned across the entire near-infrared by varying the particle size. For insight into the coupling mechanism, we also measure the electron-beam-induced response of the Mie resonances in isolated silicon nanostructures in a broad size range. Finally, we show that the silicon nanoparticles act as scatterers of the SPPs supported by the film. Our results may pave the way for using high-refractive-index dielectric nanoantennas as compact elements for manipulating highly confined SPPs.

KEYWORDS: high-refractive-index nanostructures, Mie resonances, surface plasmon polaritons, electron energy-loss spectroscopy, hybrid dielectric—plasmon resonances

urface plasmon polaritons (SPPs) supported by metal films have been the subject of intense research since their first prediction by Ritchie, as they enable the localization and guiding of light at subwavelength scales.² These properties are desirable for reducing the footprint and energy consumption of integrated photonic devices^{3,4} as well as realizing twodimensional manipulation of light.⁵ Several different passive SPP components, such as lenses, prisms, and graded-index structures, have already been realized. 6,7 However, SPPs cannot be directly excited due to the momentum mismatch between the impinging light and the SPP. The most common excitation techniques are based on either total internal reflection, such as Kretschmann or Otto prism coupling, or diffractive effects, such as grating couplers.8 While prism coupling is suitable for investigating fundamental SPP properties, it is usually bulky and not amenable to miniaturization. On the other hand, grating coupling requires patterning the metal film on a scale several times larger than the wavelength of light, which may compromise the quality of the film. This can be particularly detrimental in high-quality atomically thin materials⁹ and passivated metal films.¹⁰ These considerations have prompted an interest in launching SPPs using subwavelength light scatterers, which provide access to a broad range of momenta. In this scheme, a key parameter for achieving efficient SPP launching is a significant modal overlap between the field of the resonant nanostructure and the SPP supported by the metal film. While a broad range of different plasmonic 11,12 and dielectric 13,14 resonant nanostructures have been considered, there has been little attention on modifying

the SPP to improve the modal overlap and thereby boost the coupling to SPPs. So far, studies have focused on coupling to the SPP of optically thick metal films, whose field is not optimized to overlap with either plasmonic or dielectric nanostructures. ^{15,16}

In this work, we experimentally demonstrate that geometric Mie resonances¹⁷ supported by silicon nanoparticles hybridize strongly with the highly confined SPPs in 10-nm-thin gold films. The strong hybridization leads to the formation of a new class of hybrid dielectric—plasmon resonances, ¹⁶ where the out-of-plane confinement is enabled by the SPP, while the inplane confinement is provided by the silicon nanoparticle. Such hybrid resonances also occur for optically thick metal films, where they offer light confinement with low losses and high radiation efficiency into free-space light. ^{16,18} In contrast, the hybrid dielectric—plasmon resonance reported here has a strong modal overlap with the SPP supported by the thin gold film, providing a promising platform for efficient nanoscale plasmon generation.

We perform the experimental characterization with electron energy-loss spectroscopy (EELS) in a transmission electron

Received: October 6, 2020 Published: May 19, 2021





microscope (TEM), which can measure the optical response of nanophotonic structures with nanometer spatial resolution and meV energy resolution. ^{19,20} This powerful technique has been used to characterize the plasmonic response of a range of metal nanostructures^{21–23} as well as low-energy phonon excitations.²⁴ The simultaneous high spatial and spectral resolution enables us to perform position-dependent spectral investigation over the area of the silicon nanoparticles to characterize the hybrid dielectric-plasmon resonances as well as the Mie resonances. We present near-field profiles of the Mie resonances and map their resonance energies across a broad range of nanoparticle sizes. We show that the presence of an ultrathin gold film beneath the silicon nanoparticles produces a hybrid resonance due to SPP coupling with a nearfield profile distinctly different from those of the Mie resonances. Notably, we find that the hybrid resonance confines light on a deep-subwavelength scale of $\sim \lambda/10$ (where λ is the wavelength in free space), which is beyond the diffraction limit of silicon. The hybrid resonance and thereby the SPP excitation wavelength can be tuned across the entire near-infrared wavelength range, including telecommunication wavelengths, by varying the nanoparticle size. Finally, we exploit the capability of the electron beam to directly excite SPPs to demonstrate that silicon nanoparticles act as SPP scatterers. Our results show that silicon nanoparticles act as compact plasmon launchers and scatterers, which may enable nanoscale plasmon circuitry for on-chip applications without compromising the metal film quality.

RESULTS

Mie Resonances. The Mie resonances of silicon nanoparticles have been studied with a variety of optical techniques¹⁷ as well as cathodoluminescence, but, to the best of our knowledge, there have been no reports on their EELS response. It is therefore enlightening to first consider the EELS response of isolated silicon nanoparticles (Figure 1) before discussing the properties of the hybrid dielectricplasmon resonance. We prepare crystalline silicon nanoparticles of spherical shape in a colloidal suspension²⁷ and carefully disperse them on a thin silicon nitride membrane (Methods). This produces well-separated silicon nanoparticles with a large size distribution, which enables us to perform all the measurements on the same sample under identical experimental conditions. Figure 1b shows a typical EELS spectrum for a pristine silicon nanoparticle of radius $r = 54.6 \pm$ 1.1 nm, which is obtained by averaging the EELS signal collected at an electron beam position of approximately 20 nm outside the nanoparticle surface (Figure 1c). We observe two clear peaks in the spectrum, which are due to the excitation of Mie resonances in the silicon nanoparticle. Using an analytical theory for the EELS probability of a swift electron in the external vicinity of a vacuum-embedded dielectric sphere, 28 we identify the low-energy peak at 2.54 eV as the magnetic dipole (MD) resonance, while the high-energy peak at 2.97 eV is attributed to the electric dipole (ED) resonance. The measured resonance energies are in quantitative agreement with theory, while the experimental peaks are broadened due to the energy resolution of our EELS setup. The effect of a finite experimental energy resolution can be mimicked in the theoretical spectra by convolution with a Lorentzian function,²⁹ which broadens the EELS resonances (see Methods). As shown in Figure 1b, the convoluted spectrum

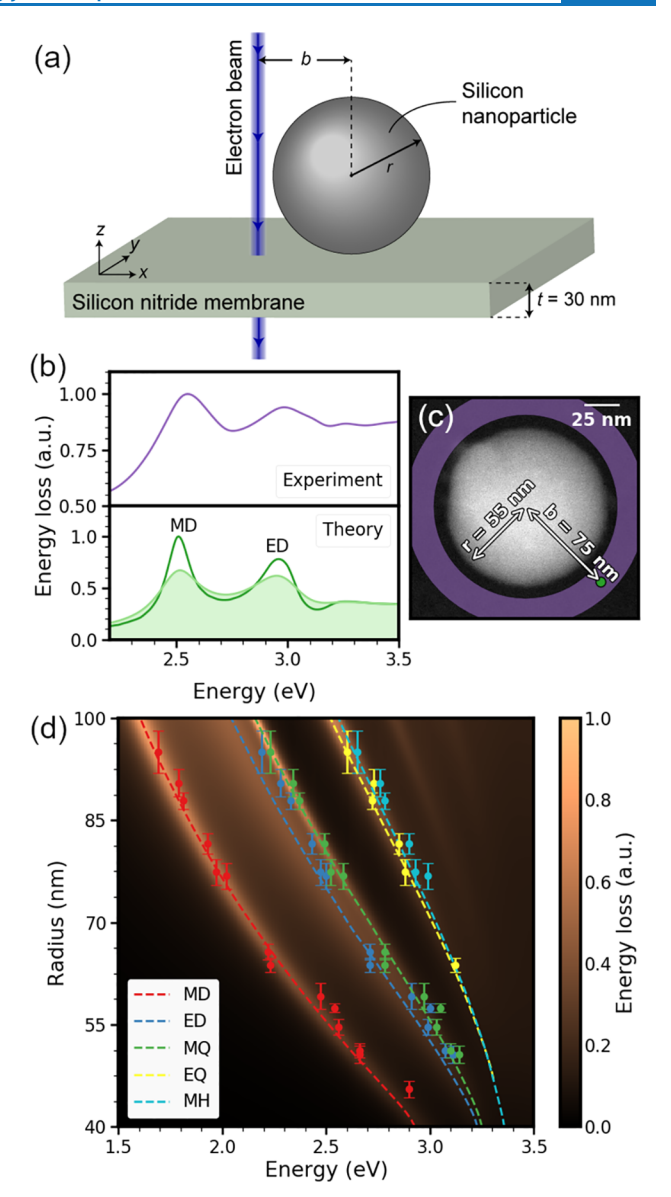


Figure 1. EELS measurements of Mie resonances in silicon nanoparticles. (a) Schematic of a silicon nanoparticle of radius r placed on a silicon nitride membrane and excited by an electron beam. The impact parameter b denotes the distance between the electron beam and the center of the nanoparticle. (b) Experimental (top) and theoretical (bottom) EELS spectra of a silicon nanoparticle with radius $r = 54.6 \pm 1.1$ nm, acquired from the electron beam positions shown in (c). The area curve represents a convolution with a Lorentzian function. (c) STEM image of the nanoparticle, where the purple region represents the integration region for the experimental spectrum and the green point depicts the location of the electron beam in the simulation. (d) Measured resonance energies as a function of particle radius for the first five Mie resonances in silicon nanoparticles. The color plot shows the EELS simulation for an impact parameter b = r + 20 nm, and the dashed curves indicate the theoretical Mie resonance energies.

captures both the resonance energies and linewidths observed in the experimental measurement.

We extend our analysis by measuring the Mie resonance energies of silicon nanoparticles over a broad size range (Figure 1d). The colored points show the experimentally measured resonance energies of the first five Mie resonances spanning a radius range from 40 to 100 nm. The color map

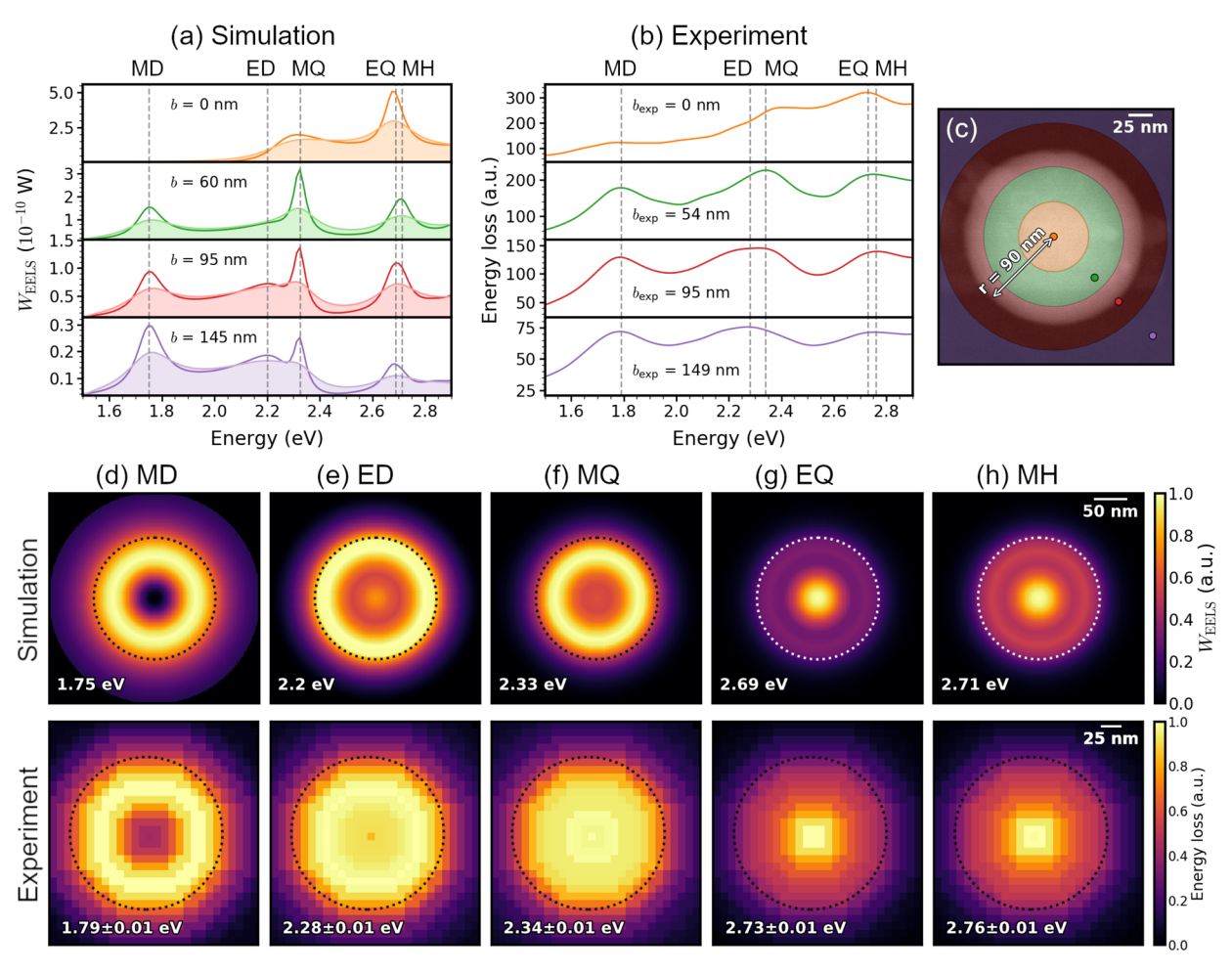


Figure 2. EELS mapping of Mie resonances. (a) Simulated EELS spectra of a silicon nanoparticle with radius r = 90 nm at different impact parameters b. The area curves depict the simulated spectra convoluted with a Lorentzian function. (b) Experimental EELS spectra for a particle with radius $r = 90.5 \pm 2.0$ nm acquired from the regions shown in (c). (c) STEM image of the nanoparticle, where the colored areas represent the integration regions for the experimental EELS signal, and the colored points are the position of the electron beam in the simulation. (d-h) Simulated (top) and experimental (bottom) EELS intensity maps of the first five Mie modes. The EELS maps are individually normalized.

depicts the calculated EELS probability using the same analytical theory as in Figure 1b, while the dashed lines show the first maxima of the different Mie scattering coefficients, which indicate the position of the resonance energies. We find excellent quantitative agreement between experiment and theory across the wide span of particle sizes, even though the theory does not account for the presence of the thin substrate. The strong match evidences that the silicon nitride membrane has a negligible influence on the Mie resonances, which is in agreement with earlier theoretical studies on the influence of substrates on Mie resonances. 30,31 In addition, we highlight that the tightly confined electromagnetic field of the electron beam couples stronger to higherorder Mie resonances than the plane-wave field used in optical measurements, 17,32 which enables us to detect them even in small particles.

The EELS signal is a measure of the efficiency to excite optical resonances by the electron beam, ²² which depends strongly on the position of the electron beam. We exploit this feature of EELS to identify the resonance energies of spectrally close Mie resonances. In particular, we distinguish the ED and magnetic quadrupole (MQ) modes as well as the electric quadrupole (EQ) and magnetic hexapole (MH) modes, even though their resonance energies are closer than the energy

resolution of our EELS setup (80 meV). In Figure 2a-c, we present EELS spectra acquired at different electron beam positions from a nanoparticle with a larger radius of $r = 90 \pm$ 2.0 nm, which supports higher-order Mie resonances. From EELS simulations (Figure 2a), we find that the ED mode is efficiently excited by positioning the electron beam outside the nanoparticle (b = 145 nm), while the MQ mode dominates for impact parameters inside the nanoparticle (b = 60 nm). This difference in excitation efficiency shifts the experimental EELS peak to either the ED or MQ resonance energies, enabling us to identify both resonance energies from each silicon nanoparticle (Figure 2b). A similar analysis is performed to distinguish the EQ and MH modes by comparing the EELS signal acquired in the center of the particle (b = 0 nm) to that acquired approximately halfway through the particle (see Figure S1 for detailed comparison). While this unique property of EELS has also been used to distinguish spectrally close plasmonic modes, 29 the strong surface localization of plasmonic fields generally requires the electron beam to be positioned near the particle surface for efficient excitation. As such, distinguishing neighboring plasmonic modes with EELS often comes down to achieving the highest energy resolution possible.³³ In contrast, Mie resonances localize light both inside and outside the nanoparticle, enabling us to fully

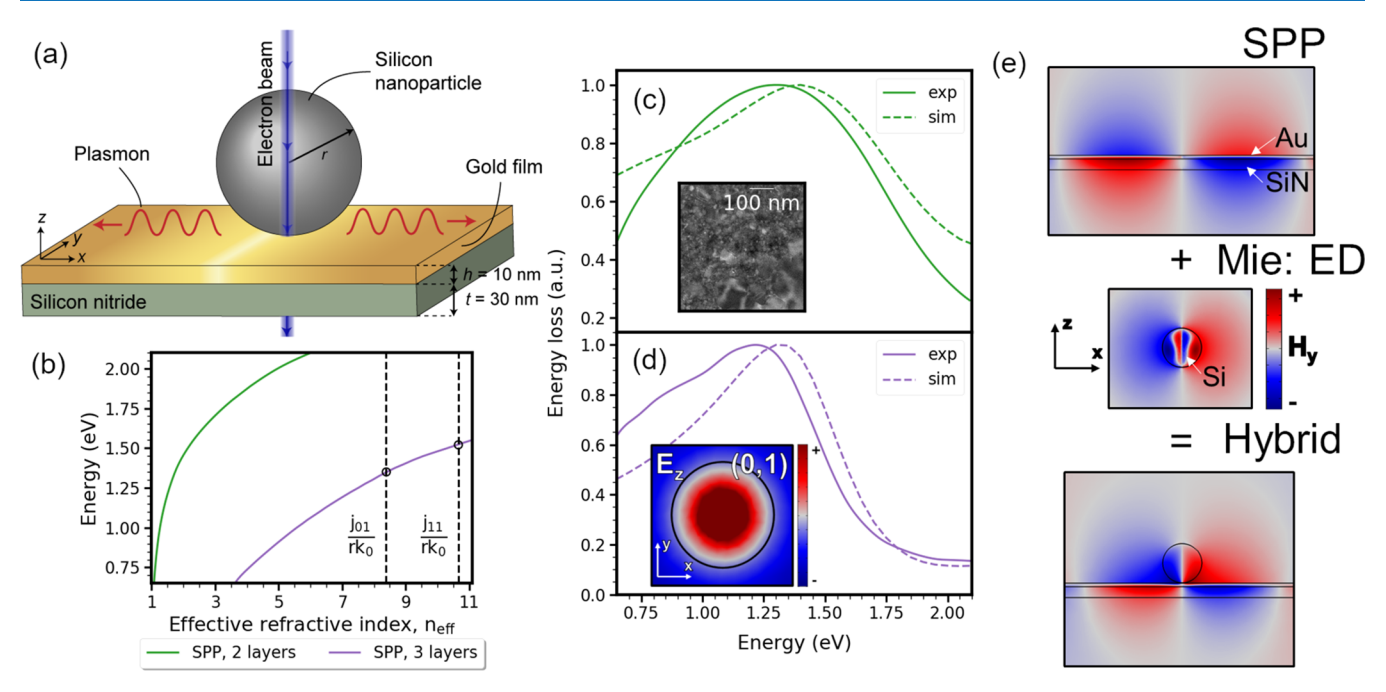


Figure 3. Hybrid dielectric—plasmon resonances. (a) Schematic of a silicon nanoparticle placed on a thin layer stack consisting of a 10 nm gold film on top of a 30 nm silicon nitride membrane. The structure is probed by an electron beam penetrating the center of the nanoparticle (b = 0 nm). (b) Dispersion relation of the short-range SPP supported by the gold—silicon nitride stack (green line) as well as the silicon—gold—silicon nitride stack (purple). In the latter, the silicon thickness is 110 nm, corresponding to the diameter of the nanoparticle. The two lowest-order resonance conditions given by eq 2 are depicted as vertical lines. (c, d) Experimental and simulated EELS spectra of the structure without and with the silicon nanoparticle, respectively. The radius of the particle is $r = 54.1 \pm 0.8$ nm. The inset in (d) shows the z component of the electric field of the (0, 1) hybrid mode in the xy-plane at the top gold surface. (e) Cross-sectional magnetic field profiles of the short-range SPP mode without the nanoparticle (top), the electric dipole mode of an isolated silicon nanoparticle (middle), and the hybrid dielectric—plasmon mode (bottom).

capitalize on the highly localized nature of the electron beam source.

The EELS simulations shown in Figure 2a are performed in COMSOL Multiphysics, which allows us to go beyond the analytical solution provided in ref 28 by including thin substrate layers as well as obtaining EELS spectra for impact parameters inside the nanoparticle. The EELS signal is calculated as the work rate $W_{\rm EELS}$ done on the electron beam by the electromagnetic field induced by the optical structure ${\bf F}^{\rm ind}$.

$$W_{\rm EELS}(\omega) = \frac{1}{2} \int \text{Re}[\mathbf{j}^*(\mathbf{r}_{\rm e}, z, \omega) \cdot \mathbf{E}^{\rm ind}(\mathbf{r}_{\rm e}, z, \omega)] \, \mathrm{d}z$$
 (1)

Here, $\mathbf{j}(\mathbf{r}_e, z, \omega) = -e\hat{\mathbf{z}}\delta(\mathbf{r} - \mathbf{r}_e)e^{i\omega z/\nu}$ is the frequency domain representation of the current density of an electron moving at a speed ν along the z-direction, and $\mathbf{r}_e = (x_e, y_e)$ denotes the inplane position of the electron beam, which relates to the impact parameter as $b = |\mathbf{r}_e|$. The integral in eq. 1 is performed along the line sustaining the incident current.

Equipped with eq 1, we map the first five Mie modes both numerically and experimentally (Figure 2d-h). We harness the near-perfect spherical shape of the nanoparticles to average the experimental data along the in-plane azimuth angle, which results in a radial EELS profile with a high signal-to-noise ratio (Methods). The radial profile is then depicted in a two-dimensional plot for easy comparison with the simulated EELS maps (see Figure S2 for the unprocessed EELS maps). The MD mode (Figure 2d) shows a doughnut-like field profile with a maximum intensity approximately two-thirds inside the nanoparticle and a complete minimum at the center. This demonstrates that the radial electric field of the electron beam cannot excite the MD mode when the electron beam is

positioned at the particle center. A similar intensity map is observed for the MQ mode (Figure 2f), albeit with a stronger localization to the nanoparticle and a weaker minimum in the center. On the other hand, the ED mode (Figure 2e) shows a peak in the center and maximal intensity localized near the particle surface. Compared to the MQ mode, the ED mode extends further outside the particle, which we exploited to distinguish their close resonance energies. The higher-order EQ and MH modes (Figure 2g,h) both show a maximal EELS intensity in the particle center. However, the MH mode decreases continuously as the position of the beam is moved radially outward, while the EQ mode shows a dip halfway through the particle. This subtle difference in excitation efficiency is utilized to distinguish their resonance energies in the experimental data. We note that the EELS maps of neighboring Mie modes are influenced by the broad nature of the resonances and, for the experimental maps, also by the energy resolution of the EELS setup (see Figure S2 for the simulated EELS maps convoluted with a Lorentzian to account for the energy resolution of the EELS setup). Nonetheless, we find reasonable agreement between experimental and simulated EELS maps, which demonstrates that EELS can be successfully applied to detect the rich field profiles of Mie

Plasmon Launching. Placing silicon nanoparticles on metal films substantially changes the optical response due to the presence of SPPs. This coupling between SPPs and Mie resonances gives rise to hybrid dielectric—plasmon resonances. For optically thick metal films, the coupling into guided SPPs is weak, and the hybrid resonances radiate primarily into free-space photons. In contrast, optically thin films support coupled SPPs which have a strong modal overlap with the

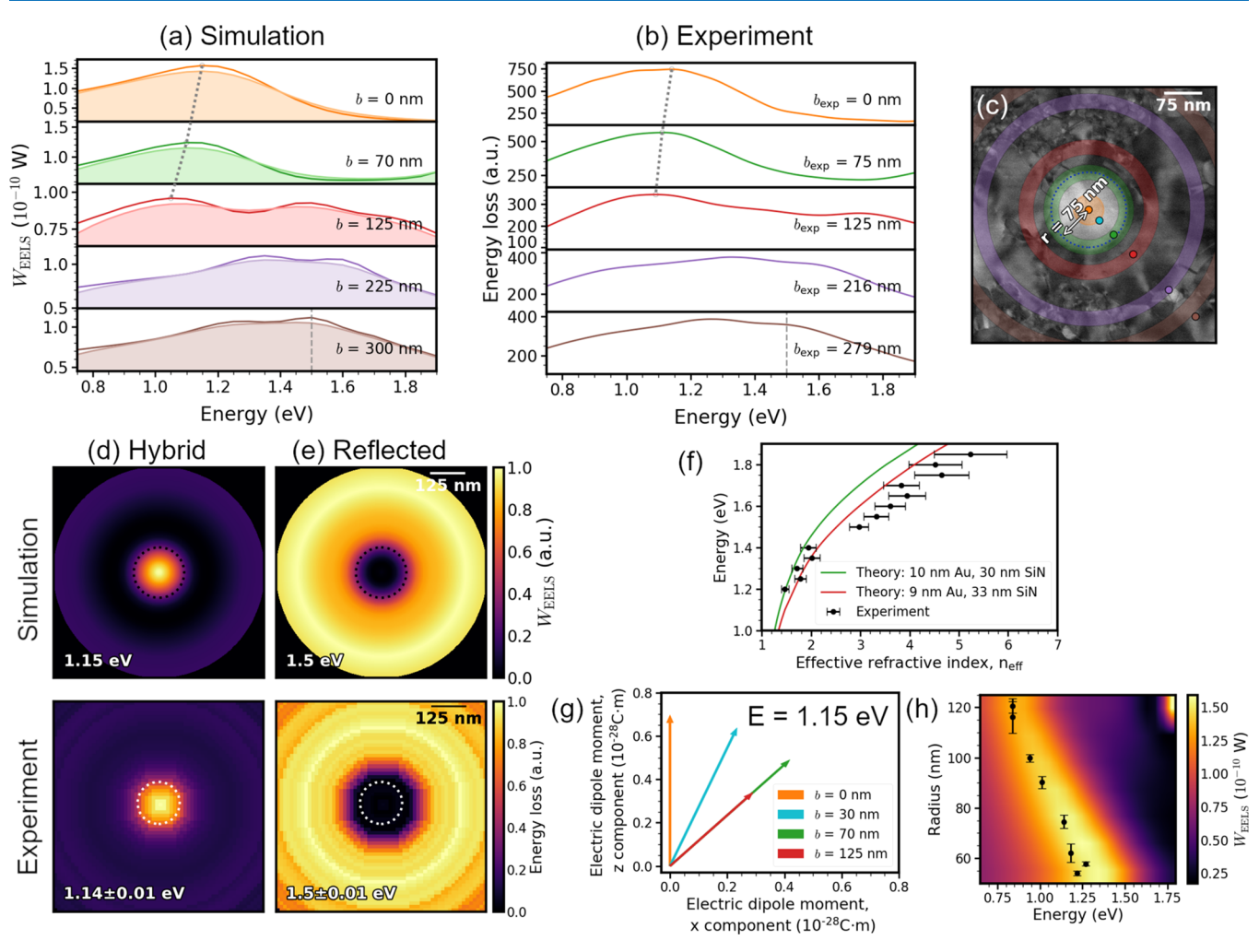


Figure 4. Plasmon launching and scattering. (a) Simulated EELS spectra of a silicon nanoparticle (r = 75 nm) on a thin gold—silicon nitride stack at different impact parameters b. The area curves depict the simulated spectra convoluted with a Lorentzian function. (b) Experimental EELS spectra for a particle with radius $r = 74.5 \pm 2.6$ nm acquired from the regions shown in (c). (c) STEM image of the nanoparticle, where the colored areas represent the integration regions for the experimental EELS signal, and the colored points are the position of the electron beam in the simulation. (d, e) Simulated (top) and experimental (bottom) EELS maps of the (0, 1) hybrid mode and the SPP reflection. (f) Experimental and theoretical dispersion relations of the short-range SPP supported by the gold—silicon nitride stack. Experimental data points are determined by using eq 3 on the SPP reflection EELS maps of the nanoparticle in (c). (g) Electric dipole moment of the (0, 1) hybrid mode at different impact parameters, which shows the change in dipole direction as the electron beam is moved away from the center of the particle. (h) Measured resonance energies of the (0, 1) hybrid mode as a function of particle radius acquired by positioning the electron beam in the nanoparticle center. The color plot shows the EELS simulation for an impact parameter of b = 0 nm.

hybrid resonance. Consequentially, the coupling into SPPs is boosted (see Figure S5). We construct such hybrid dielectricplasmon resonances by placing silicon nanoparticles on a gold film of only 10 nm thickness (Figure 3a). The gold film is deposited on the silicon nitride membrane using an APTMS adhesion layer, which produces high-quality thin films with negligible influence on the SPP propagation³⁵ (Methods). In general, thin metal films can support two SPP modes, commonly referred to as the long-range and short-range SPPs, due to the hybridization of the SPPs at each metal surface. However, the asymmetric dielectric environment of our gold film turns the long-range SPP into a leaky mode,⁵ while the short-range SPP remains below the light line and is strongly confined to the gold film (Figure 3b, green line). The short-range SPP can be excited directly by the electron beam without the nanoparticle, resulting in a broad response in the EELS spectrum with a peak at 1.3 eV (Figure 3c). The large linewidth (~1 eV) of the EELS peak stems from the

broadband nature of the electron source, which may couple to the SPP at different energies and wavenumbers. This property combined with the dispersion relation of the short-range SPP specifies the peak energy in the EELS spectrum.³⁶

On the other hand, the presence of the silicon nanoparticle gives rise to a notably narrow and red-shifted EELS peak (Figure 3d). The EELS peak is due to the formation of a hybrid dielectric—plasmon resonance, which, for the particle radius of $r = 54.1 \pm 0.8$ nm, has a resonance energy of 1.22 eV. The hybrid resonance can be conceptually understood as a standing wave of the short-range SPP residing beneath the nanoparticle. The SPP dispersion relation is influenced by the local presence of silicon and can to a good approximation be accounted for in a three-layer silicon—gold—silicon nitride model, where the thickness of the silicon layer is defined by the particle diameter (Figure 3b, purple line). The dispersion relation is then sampled at specific wavenumbers k_{lm} defined by

the resonance condition of zero round trip phase, ¹⁶ which is given by the relation

$$k_{lm}r \approx j_{lm} \tag{2}$$

Here, j_{lm} denotes the mth zero of the spherical Bessel function of order l. Physically, the indices (l, m) correspond to the field variations in the radial and azimuthal directions, respectively. The two lowest quantized wavenumbers given by eq 2 are depicted in Figure 3b. We find that the resonance energy of the lowest-order (0, 1) mode, corresponding to the field profile shown in Figure 3d, matches accurately with the energy of the EELS peak in our measurements. The nature of the hybrid resonance is further elucidated in Figure 3e, which illustrates how the short-range SPP of the thin gold film hybridizes with the out-of-plane ED resonance of the silicon nanoparticle to form the hybrid resonance. Here, it is of value to note the similarity in the field profiles of the hybrid mode and the SPP mode. This substantial spatial field overlap facilitates an efficient excitation of the SPP mode.

Another signature of the strong hybridization is the spectral shift between the ED resonance of an isolated silicon nanoparticle (Figure 1b) and the hybrid resonance. Comparing silicon nanoparticles of the same size, the ED resonance of an isolated silicon nanoparticle shows a dramatic shift from 2.97 eV to the hybrid resonance energy of 1.22 eV. Consequentially, the hybrid resonance confines light on a scale even smaller than the lowest-order MD resonance, which is not altered significantly by the presence of the thin gold film (see Figure S3). Comparing the hybrid resonance wavelength $\lambda_{\rm H}$ with the MD resonance wavelength λ_{MD} of the same particle reveals an increase in light confinement by a factor $\lambda_{\rm H}/\bar{\lambda}_{\rm MD}\approx 2$. The gain in light confinement stems from the fact that the hybrid resonance is formed due to the confinement of the SPP, while the Mie resonances arise due to the confinement of light inside silicon. Interestingly, this reveals that dielectric nanoparticles on thin metal films lead to a system with substantially higher effective refractive index than that available with purely dielectric materials, offering a route for shrinking dielectric scatterers below their diffraction limit.

The resonance energy of the hybrid mode is surprisingly dependent on the position of the electron beam (Figure 4), which is in contrast to the Mie resonances of isolated silicon nanoparticles (Figure 2). We observe that as the electron beam is moved radially outward from the center of the silicon nanoparticle, the hybrid resonance energy shows a red-shift of around 50 nm (Figure 4a-c). A Cartesian multipole decomposition³⁷ of the electromagnetic field induced by the electron beam reveals that the hybrid mode can be described by an electric dipole (Figure 4g). When the beam is positioned in the center of the particle, the electric dipole is oriented normal to the gold surface. As the beam is moved off-center, the red-shift of the hybrid mode is accompanied by a tilting of the electric dipole toward the gold surface. For impact parameters far away from the nanoparticle ($b \gtrsim 200$ nm), the EELS signal from the hybrid mode is not detected. This is also visible from the EELS maps of the hybrid mode (Figure 4d), which are different from the Mie modes of isolated silicon nanoparticles (Figure 2).

In addition to the dependence of the electron beam position, eq 2 reveals that the resonance energy of the hybrid modes can be tuned by changing the particle size. By collecting EELS data from different particles, we experimentally trace the (0, 1) mode energy as a function of particle size (Figure 4h). We find

that the resonance energy can be effectively modulated from the near-infrared to telecommunication wavelengths. The resonance energies are in agreement with our EELS simulations, which also show a line width narrowing of the resonance at lower energies due to increasing SPP propagation length.

The hybridization between the Mie and the SPP modes is a key signature of their modal overlap and needs to be tailored to effectively use silicon nanoparticles as SPP launchers. In this regard, EELS offers a unique insight into the hybridization, as we can track both spectral shifts in a large energy range and changes in the near-field profiles of the modes. Such insight is not feasible in a standard far-field optical measurement. While our EELS results are important for near-field excitation sources, such as an electron beam or dipole emitter, it is also relevant to consider the properties of our system when excited by a plane wave. To this end, we perform additional planewave simulations of the scattering efficiency of the silicon nanoparticle, which are representative for optical measurements (see Figure S4). These simulations reveal that light couples to the (1, 1) hybrid mode. By decomposing the scattered field into free-space and SPP radiation,³⁸ we find that the main contribution (>80%) to the scattering efficiency is the launching of SPPs. We also note that sending light at different angles of incidence provides a knob to fine-tune the SPP launching energy due to the reorientation of the electric dipole (Figure 4g), albeit with a reduction in the SPP coupling efficiency. This demonstrates that the hybrid dielectricplasmon modes offer efficient nanoscale SPP launching regardless of the excitation source.

Plasmon Scattering. When the electron beam is positioned outside the particle, we observe additional peaks in the EELS spectra appearing at larger energies than the hybrid mode (Figure 4a,b). These peaks occur due to the reflection of the SPP from the silicon nanoparticle. As discussed in relation to Figure 3, the electron beam can directly excite SPPs in a broad energy range,³⁹ which are subsequently reflected by the nearby silicon nanoparticle. This results in an SPP interference pattern outside the nanoparticle with local electric field maxima producing regions of EELS signal with a larger amplitude. 40 We visualize this effect by mapping the EELS intensity at an energy of 1.5 eV (Figure 4e). Here, a clear ring structure is visible with a maximum EELS intensity approximately 200 nm from the nanoparticle center, which is in good agreement with the EELS simulations. The radial distance b from the EELS maximum to the nanoparticle center can be determined by tracking the SPP propagation and reflection phases,²² providing physical insight into the simulations. By describing the SPP waves as one-dimensional plane waves with a wavelength λ_{SPP} , we find the phase relation

$$b = \frac{(2\pi q - \phi)}{4\pi} \lambda_{\text{SPP}} \tag{3}$$

Here, ϕ is the reflection phase and q is a positive integer, which denotes the interference order. From EELS simulations we find that the SPP reflection occurs at the nanoparticle center (see Figure S6). A part of the SPP propagation phase is therefore acquired inside the nanoparticle, which differs from the phase pickup outside the nanoparticle due to the refractive index of silicon. In the derivation of eq 3, we have assumed that this difference in phase pickup is small and described the nanoparticle as a reflecting boundary located at the nano-

particle center. As we show, this assumption is valid at low energies where the SPP wavelength is long.

By measuring the distance b from the ring-shaped EELS maps at different energies, we extract the SPP dispersion relation using eq 3 assuming a zero phase shift upon reflection (Figure 4f). For energies below approximately 1.5 eV, the ringshaped EELS signal occurs due to the standing wave of half the SPP wavelength (q = 1), while for larger energies the standing wave corresponds to one SPP wavelength (q = 2) (see Figure S6). The experimentally extracted SPP dispersion agrees well with theory at low energies, but deviates at higher energies, even when we consider different layer thicknesses within our fabrication tolerance. Similar results are obtained when we extract the SPP dispersion from other nanoparticle sizes. The difference between theory and experiments observed at higher energies is due to the additional phase pickup upon propagation inside the nanoparticle, which is not accounted for in eq 3. Nonetheless, the SPP dispersion diagram demonstrates that silicon nanoparticles reflect the short-range SPP in a broad energy range.

At the resonance energy of the hybrid mode, the SPP reflection phase is expected to vary significantly due to the excitation of the hybrid resonance. To study this in more detail, we have simulated the SPP reflection from a silicon nanowire, which corresponds to the two-dimensional version of our system and also supports hybrid modes (see Figure S7). Here, we launch SPPs and detect the reflected SPP at the nanowire center. These simulations reveal that the SPP excitation of the hybrid mode coincides with both a varying reflection phase and an SPP reflectance minimum. The drop in the SPP reflectance is due to scattering of the SPP into freespace radiation through the hybrid mode. While we are not able to extract the reflection phase from our EELS measurements, we seem to qualitatively observe a weak drop in the EELS intensity of the interference pattern outside the nanoparticle at approximately 1.45 eV, which is close to the resonance energy of the (1, 1) hybrid mode (see Figure S8). However, an unambiguous experimental demonstration of the SPP scattering into free-space radiation due to the nanoparticle requires detecting the scattered light, such as in cathodoluminescence. Our EELS results show that silicon nanoparticles can be used to excite and reflect SPPs. This provides an exciting opportunity to design compact SPP optical elements with highrefractive-index nanostructures.

DISCUSSION AND CONCLUSIONS

Using EELS, we have measured and mapped the Mie resonances of spherical silicon nanoparticles in a broad radius range. Each Mie resonance shows unique field variations inside the nanoparticles, which we exploit in our EELS measurements. By careful positioning of the electron beam, we extract the resonance energies of the first five Mie resonances, even though some of the resonances are closer in energy than the energy resolution of our EELS setup. Full-wave EELS simulations corroborate our experimental findings and show excellent quantitative agreement. Our results expand the capabilities of EELS to include high-index nanophotonics and may in the future shed more light on important interference phenomena such as anapole states and bound states in the continuum.

By placing silicon nanoparticles on a thin gold film, we find a new class of hybrid dielectric—plasmon resonances governed by both the short-range SPP of the gold film and the nanoparticle material and size. The observed hybrid mode shows significantly stronger light confinement than the Mie resonances and couples efficiently to the SPP of the thin film. We experimentally demonstrate that the hybrid resonance energy can be controlled across the entire near-infrared by the particle size, providing a simple tuning mechanism to excite SPPs at a desired wavelength. By performing a multipole decomposition of the induced field, we find that the optical response of the hybrid mode corresponds to an electric dipole with a direction sensitive to the electron beam position. Positioning the beam in the nanoparticle center leads to an out-of-plane electric dipole moment, which is gradually tilted toward the gold surface as the beam is moved radially outward. This tilting is accompanied by a red-shift of the hybrid mode. We anticipate that the tilted electric dipole can be exploited in an optical setup to realize directional SPP launching by exciting the nanoparticle with circularly polarized light.⁴³

Finally, we experimentally show that the short-range SPPs are scattered by the nearby silicon nanoparticle. The scattering process leads to an interference pattern with local field maxima producing regions of the EELS signal with a larger amplitude. By tracking the SPP propagation and reflection, we derive a simple theoretical relation, which enables us to experimentally extract the SPP dispersion relation in a broad energy range. Our results provide evidence for the SPP scattering properties of high-index nanostructures, opening up an avenue for new designs of SPP optical elements.

METHODS

Fabrication. TEM Membranes. A low-stress silicon-rich nitride layer is deposited on top of an n-type (phosphor) (100) double-side polished silicon wafer by low-pressure chemical vapor deposition (LPCVD). The resulting thickness determined by ellipsometry is around 33 nm, with a 1 nm native silicon oxide below the nitride. This is followed by a UV lithography step to create a photoresist pattern for the membrane windows on one side of the wafer. Afterward, the silicon nitride is dry etched using the lithographic pattern, followed by photoresist strip, wet KOH etching of the silicon, and water/HCl 4:1 cleaning.

For the gold samples, the wafers are submerged into a solution of 95% isopropanol, 2.5% water, and 2.5% APTMS for 3 h to achieve a 1 nm APTMS layer, 35 followed by two steps of isopropanol/water rinsing. Sputter deposition is used to produce a 10 nm thick gold layer. Both AFM and ellipsometry confirm the thickness of the gold layer to be 9–10 nm. The root mean squared roughness of the gold surface as measured by AFM is around 1.5 nm.

The wafers are then covered with a protective layer of photoresist. The wafer without (with) gold is laser cut (diced) into smaller TEM chips. Subsequently, the photoresist is removed in acetone followed by isopropanol for 10 min in both steps. The wafers without gold are also plasma ashed for 5 min. The plasma ashing and laser cutting are not performed on the gold samples due to damage introduced to the thin gold layer by these procedures.

Silicon Nanoparticles. The crystalline silicon nanoparticles of spherical shape are produced by thermal annealing of silicon suboxide (SiO_x) and extraction into methanol. A silicon-rich SiO_x film of 10–20 μ m in thickness is prepared by cosputtering of Si and SiO₂ together with B₂O₃ and P₂O₅. The film is annealed at 1500 °C in a nitrogen atmosphere for 30 min to grow silicon nanoparticles in a SiO₂ matrix. The silicon

nanoparticles are extracted from the matrix by hydrofluoric acid (46 wt %) etching and transferred to a methanol solution. The doping of boron and phosphor results in formation of a heavily boron and phosphor codoped layer on the nanoparticle surface and prevents agglomeration in the solution. In optical measurement, it has been shown that the scattering spectrum of the nanoparticle perfectly agrees with the Mie theory. At the end of the fabrication, a 10 μ L solution of silicon nanoparticles in methanol is drop-casted onto the membrane. The membrane is nitrogen dried after a 1 min wait time.

Image Analysis. The sizes of the silicon nanoparticles are determined from the STEM images using image processing operations with the Python scikit-image library. Initially, the particle size is predetermined manually resulting in an expected radius $r_{\rm exp}$. For the samples without the gold layer, a Canny filter with $\sigma=3$ pixels is applied to find the particle edges. This is followed by a diameter $0.7r_{\rm exp}$ and area $1.4\pi r_{\rm exp}$ opening morphological operations to remove the false edge pixels.

For the samples with the gold layer, the particle edges are predetermined with a $\sigma=20$ pixels Canny edge detector. Knowing that the particle is located approximately in the center of the image (particle center coordinates c_x and c_y are in the center of the image), all the edges after $2r_{\rm exp}$ are removed. The resulting edge map is fitted with the Hough circle transform, resulting in the intermediate radius $r_{\rm int}$ and intermediate particle center coordinates c_{xi} and c_{yi} . Then, the particle edges are found with a $\sigma=10$ pixels Canny edge detector. Assuming the particle center is located at c_{xi} and c_{yi} all edges before $0.8r_{\rm int}$ and after $1.3r_{\rm int}$ are removed, followed by a diameter $0.1r_{\rm exp}$ opening. Finally, the Hough circle transform is applied on the last edge map to find the best fit for the radius and particle center.

The uncertainty in the radius is determined by fitting the number of intersections-radius dependence with a bimodal distribution of 2 Gaussians. The number of intersectionsradius dependence is provided from the Hough circle transform since it draws circles with a particular radius centered on each pixel of the edge map and counts the number of their intersections at different locations on the map. The point with the highest number is taken as a center location of the particle. This process is performed for different radii in the provided radius range $r_{\rm exp} \pm r_{\rm range}$. The uncertainty is taken as the standard deviation of the smaller Gaussian or the image resolution if the resolution is larger than the standard deviation. Then, the final edge map is enlarged by 2 pixels, the circle Hough transform is performed, and Gaussians are fitted again, resulting in the new circle parameters and the uncertainty. If the uncertainty is smaller than the previous value and not larger than the image resolution of 3 pixels, it is taken as a new true value; otherwise, the previous values are preserved. This procedure can be repeated multiple times, resulting in edges that are increased by 2 pixels every step.

EELS Measurements and Analysis. The EELS measurements are performed in a monochromated and aberration-corrected FEI Titan operated in STEM mode at an acceleration voltage of 300 kV, providing a probe size of ~0.5 nm and an energy resolution of 0.08 eV (as measured by the full-width at half-maximum of the zero-loss peak). The zero-loss peak is removed using Richardson—Lucy deconvolution. As input for the point-spread function, we use the reflected tail method for samples without gold, while for the samples with gold we used an EELS spectrum obtained in a vacuum. Due to a small asymmetry in the zero-loss peak, the

deconvolution algorithm produced an artificial EELS peak in the energy range below 0.6 eV. However, the artificial peak did not overlap with any of the observed resonances and could be safely removed using a first-order logarithmic polynomial.

The depicted EELS spectra are obtained by integrating the deconvoluted EELS data around the experimental impact parameter $b_{\rm exp}$. For the disk-shaped integration regions, the experimental impact parameter denotes the center of the disk. For the annulus-shaped regions, the experimental impact parameter denotes the mean of the inner and outer radii. The depicted EELS spectra are smoothed with a Gaussian function ($\sigma = 0.03 \text{ eV}$).

The EELS maps are obtained by summing the deconvoluted EELS data in a spectral window of 0.02 eV width centered at the resonance energies. In order to improve the signal-to-noise ratio, the map was spatially binned, reducing the effective number of pixels by a factor of 2 in each row and column, i.e., a factor of 4 in total. Afterward, a Gaussian filter with $\sigma=0.8$ pixels was applied to smooth the image. Exploiting the spherical symmetry of the nanoparticles, the maps are integrated along the azimuth angle at the coordinates located at the same distance from the nanoparticle center.

EELS Simulations. The EELS simulations are performed in COMSOL Multiphysics, which uses finite-element modeling to solve Maxwell's equations. The electron beam is simulated using an edge current with an amplitude of 1 μ A. The induced electromagnetic field is determined by calculating the field with and without the optical structures in the simulation space and subsequently subtracting them. Using the obtained induced electric field, the energy loss can be calculated using eq 1. To mimic the experimental energy resolution, we also perform a convolution with a Lorentzian function with a full-width at half-maximum of 0.1 eV. The complex refractive indices for silicon, gold, and silicon nitride are taken from refs 44–46, respectively. The silicon nitride layer is not included in the simulation of the silicon nanoparticle without the gold layer (Figure 2).

ASSOCIATED CONTENT

Supporting Information

The Supporting Information is available free of charge at https://pubs.acs.org/doi/10.1021/acsphotonics.0c01554.

Positioning of the electron beam for distinguishing the spectrally close EQ and MH Mie resonances; additional spatial EELS maps for Figure 2; EELS measurements of Mie resonances in silicon nanoparticles on a thin gold film; plane-wave excitation of the hybrid dielectric—plasmon mode at varying angles of incidence; SPP coupling efficiency of the hybrid dielectric—plasmon mode as a function of gold thickness; SPP reflection for different interference orders (PDF)

AUTHOR INFORMATION

Corresponding Author

Søren Raza — Department of Physics, Technical University of Denmark, DK-2800 Kongens Lyngby, Denmark; orcid.org/0000-0002-0296-7202; Email: sraz@dtu.dk

Authors

Artyom Assadillayev – Department of Physics, Technical University of Denmark, DK-2800 Kongens Lyngby, Denmark

- **Tatsuki Hinamoto** Department of Electrical and Electronic Engineering, Kobe University, Kobe 657-8501, Japan
- Minoru Fujii Department of Electrical and Electronic Engineering, Kobe University, Kobe 657-8501, Japan; orcid.org/0000-0003-4869-7399
- Hiroshi Sugimoto Department of Electrical and Electronic Engineering, Kobe University, Kobe 657-8501, Japan; orcid.org/0000-0002-1520-0940
- Mark L. Brongersma Geballe Laboratory for Advanced Materials, Stanford University, Stanford, California 94305, United States; Occid.org/0000-0003-1777-8970

Complete contact information is available at: https://pubs.acs.org/10.1021/acsphotonics.0c01554

Author Contributions

S.R. and M.L.B. conceived the experiments. A.A. fabricated the samples and performed the EELS measurements. A.A. performed the image and EELS data analyses. A.A. and S.R performed the simulations. T.H., H.S., and M.J. fabricated the silicon nanoparticles. A.A. and S.R. prepared figures and wrote the manuscript. S.R. supervised the project. All authors discussed the results and contributed to the preparation of the manuscript.

Notes

The authors declare no competing financial interest.

ACKNOWLEDGMENTS

We thank Joachim Dahl Thomsen and Radu Malureanu for assisting with the fabrication of the TEM chips and the deposition of the gold film, respectively. We thank Tim Booth for fruitful discussions. S.R. and A.A. acknowledge support by the Independent Research Funding Denmark (7026-00117B).

■ REFERENCES

- (1) Ritchie, R. H. Plasma losses by fast electrons in thin films. *Phys. Rev.* 1957, 106, 874–881.
- (2) Schuller, J. A.; Barnard, E. S.; Cai, W.; Jun, Y. C.; White, J. S.; Brongersma, M. L. Plasmonics for extreme light concentration and manipulation. *Nat. Mater.* **2010**, *9*, 193–204.
- (3) Cheben, P.; Halir, R.; Schmid, J. H.; Atwater, H. A.; Smith, D. R. Subwavelength integrated photonics. *Nature* **2018**, *560*, *565*–*572*.
- (4) Haffner, C.; et al. Low-loss plasmon-assisted electro-optic modulator. *Nature* **2018**, *556*, 483–486.
- (5) Han, Z.; Bozhevolnyi, S. I. Radiation guiding with surface plasmon polaritons. *Rep. Prog. Phys.* **2013**, *76*, 016402.
- (6) Bozhevolnyi, S. I.; Pudonin, F. A. Two-dimensional micro-optics of surface plasmons. *Phys. Rev. Lett.* **1997**, *78*, 2823–2826.
- (7) Hohenau, A.; Krenn, J. R.; Stepanov, A. L.; Drezet, A.; Ditlbacher, H.; Steinberger, B.; Leitner, A.; Aussenegg, F. R. Dielectric optical elements for surface plasmons. *Opt. Lett.* **2005**, *30*, 893.
- (8) Zayats, A. V.; Smolyaninov, I. I.; Maradudin, A. A. Nano-optics of surface plasmon polaritons. *Phys. Rep.* **2005**, *408*, 131–314.
- (9) Basov, D. N.; Fogler, M. M.; García de Abajo, F. J. Polaritons in van der Waals materials. *Science* **2016**, 354, aag1992.
- (10) Wang, Y.; Yu, J.; Mao, Y. F.; Chen, J.; Wang, S.; Chen, H. Z.; Zhang, Y.; Wang, S. Y.; Chen, X.; Li, T.; Zhou, L.; Ma, R. M.; Zhu, S.; Cai, W.; Zhu, J. Stable, high-performance sodium-based plasmonic devices in the near-infrared. *Nature* **2020**, *581*, 401–405.
- (11) Smolyaninov, I. I.; Mazzoni, D. L.; Davis, C. C. Imaging of surface plasmon scattering by lithographically created individual surface defects. *Phys. Rev. Lett.* **1996**, *77*, 3877–3880.
- (12) Liu, Y.; Palomba, S.; Park, Y.; Zentgraf, T.; Yin, X.; Zhang, X. Compact magnetic antennas for directional excitation of surface plasmons. *Nano Lett.* **2012**, *12*, 4853–4858.

- (13) Landreman, P. E.; Brongersma, M. L. Deep-subwavelength semiconductor nanowire surface plasmon polariton couplers. *Nano Lett.* **2014**, *14*, 429–434.
- (14) Sinev, I.; Komissarenko, F.; Iorsh, I.; Permyakov, D.; Samusev, A.; Bogdanov, A. Steering of guided light with dielectric nanoantennas. *ACS Photonics* **2020**, *7*, 680–686.
- (15) Yang, Y.; Zhen, B.; Hsu, C. W.; Miller, O. D.; Joannopoulos, J. D.; Soljačić, M. Optically thin metallic films for high-radiative-efficiency plasmonics. *Nano Lett.* **2016**, *16*, 4110–4117.
- (16) Yang, Y.; Miller, O. D.; Christensen, T.; Joannopoulos, J. D.; Soljačić, M. Low-loss plasmonic dielectric nanoresonators. *Nano Lett.* **2017**, *17*, 3238–3245.
- (17) Kuznetsov, A. I.; Miroshnichenko, A. E.; Brongersma, M. L.; Kivshar, Y. S.; Luk'yanchuk, B. Optically resonant dielectric nanostructures. *Science* **2016**, *354*, aag2472.
- (18) Sugimoto, H.; Fujii, M. Broadband dielectric-metal hybrid nanoantenna: Silicon nanoparticle on a mirror. *ACS Photonics* **2018**, *5*, 1986–1993.
- (19) Egerton, R. F. Electron energy-loss spectroscopy in the TEM. Rep. Prog. Phys. 2009, 72, 016502.
- (20) García de Abajo, F. J. Optical excitations in electron microscopy. Rev. Mod. Phys. 2010, 82, 210-256.
- (21) Nelayah, J.; Kociak, M.; Stéphan, O.; García de Abajo, F. J.; Tencé, M.; Henrard, L.; Taverna, D.; Pastoriza-Santos, I.; Liz-Marzán, L. M.; Colliex, C. Mapping surface plasmons on a single metallic nanoparticle. *Nat. Phys.* **2007**, *3*, 348–353.
- (22) Raza, S.; Esfandyarpour, M.; Koh, A. L.; Mortensen, N. A.; Brongersma, M. L.; Bozhevolnyi, S. I. Electron energy-loss spectroscopy of branched gap plasmon resonators. *Nat. Commun.* **2016**, *7*, 13790.
- (23) Smith, K. C.; Olafsson, A.; Hu, X.; Quillin, S. C.; Idrobo, J. C.; Collette, R.; Rack, P. D.; Camden, J. P.; Masiello, D. J. Direct observation of infrared plasmonic Fano antiresonances by a nanoscale electron probe. *Phys. Rev. Lett.* **2019**, *123*, 177401.
- (24) Govyadinov, A. A.; Konečná, A.; Chuvilin, A.; Vélez, S.; Dolado, I.; Nikitin, A. Y.; Lopatin, S.; Casanova, F.; Hueso, L. E.; Aizpurua, J.; Hillenbrand, R. Probing low-energy hyperbolic polaritons in van der Waals crystals with an electron microscope. *Nat. Commun.* **2017**, *8*, 95.
- (25) Coenen, T.; van de Groep, J.; Polman, A. Resonant modes of single silicon nanocavities excited by electron irradiation. *ACS Nano* **2013**, *7*, 1689–1698.
- (26) McPolin, C. P.; Marino, G.; Krasavin, A. V.; Gili, V.; Carletti, L.; de Angelis, C.; Leo, G.; Zayats, A. V. Imaging electric and magnetic modes and their hybridization in single and dimer AlGaAs nanoantennas. *Adv. Opt. Mater.* **2018**, *6*, 1–6.
- (27) Sugimoto, H.; Fujii, M. Colloidal dispersion of subquarter micrometer silicon spheres for low-loss antenna in visible regime. *Adv. Opt. Mater.* **2017**, *5*, 1–8.
- (28) García de Abajo, F. J. Relativistic energy loss and induced photon emission in the interaction of a dielectric sphere with an external electron beam. *Phys. Rev. B: Condens. Matter Mater. Phys.* 1999, 59, 3095–3107.
- (29) Raza, S.; Kadkhodazadeh, S.; Christensen, T.; di Vece, M.; Wubs, M.; Mortensen, N. A.; Stenger, N. Multipole plasmons and their disappearance in few-nanometre silver nanoparticles. *Nat. Commun.* **2015**, *6*, 8788.
- (30) Markovich, D. L.; Ginzburg, P.; Samusev, A. K.; Belov, P. A.; Zayats, A. V. Magnetic dipole radiation tailored by substrates: numerical investigation. *Opt. Express* **2014**, 22, 10693.
- (31) Sugimoto, H.; Hinamoto, T.; Fujii, M. Forward to backward scattering ratio of dielectric-metal heterodimer suspended in almost free-space. *Adv. Opt. Mater.* **2019**, *7*, 1900591.
- (32) Zywietz, U.; Evlyukhin, A. B.; Reinhardt, C.; Chichkov, B. N. Laser printing of silicon nanoparticles with resonant optical electric and magnetic responses. *Nat. Commun.* **2014**, *5*, 3402.
- (33) Bellido, E. P.; Rossouw, D.; Botton, G. A. Toward 10 meV electron energy-loss spectroscopy resolution for plasmonics. *Microsc. Microanal.* **2014**, 20, 767–778.

- (34) Koh, A. L.; Fernández-Domínguez, A. I.; McComb, D. W.; Maier, S. A.; Yang, J. K. W. High-resolution mapping of electron-beam-excited plasmon modes in lithographically defined gold nanostructures. *Nano Lett.* **2011**, *11*, 1323–1330.
- (35) Sukham, J.; Takayama, O.; Lavrinenko, A.; Malureanu, R. High-quality ultrathin gold layers with an APTMS adhesion for optimal performance of surface plasmon polariton-based devices. ACS Appl. Mater. Interfaces 2017, 9, 25049–25056.
- (36) Bolton, J. P. R.; Chen, M. Electron energy loss in multilayered slabs. I. Normal incidence. *J. Phys.: Condens. Matter* **1995**, *7*, 3373.
- (37) Evlyukhin, A. B.; Fischer, T.; Reinhardt, C.; Chichkov, B. N. Optical theorem and multipole scattering of light by arbitrarily shaped nanoparticles. *Phys. Rev. B: Condens. Matter Mater. Phys.* **2016**, 94, 205434.
- (38) Yang, J.; Hugonin, J. P.; Lalanne, P. Near-to-far field transformations for radiative and guided waves. *ACS Photonics* **2016**, 3, 395–402.
- (39) Schilder, N. J.; Agrawal, H.; Garnett, E. C.; Polman, A. Phase-Resolved Surface Plasmon Scattering Probed by Cathodoluminescence Holography. *ACS Photonics* **2020**, *7*, 1476–1482.
- (40) Schoen, D. T.; Atre, A. C.; García-Etxarri, A.; Dionne, J. A.; Brongersma, M. L. Probing complex reflection coefficients in one-dimensional surface plasmon polariton waveguides and cavities using STEM EELS. *Nano Lett.* **2015**, *15*, 120–126.
- (41) Kruk, S.; Kivshar, Y. Functional meta-optics and nanophotonics governed by Mie resonances. ACS Photonics 2017, 4, 2638–2649.
- (42) Hsu, C. W.; Zhen, B.; Stone, A. D.; Joannopoulos, J. D.; Soljačić, M. Bound states in the continuum. *Nat. Rev. Mater.* **2016**, *1*, 16048.
- (43) Rodríguez-Fortuño, F. J.; Martínez, A.; Wurtz, G. A.; Zayats, A. V. Near-field interference for the unidirectional excitation of electromagnetic guided modes. *Science* **2013**, *340*, 328–331.
- (44) Aspnes, D. E.; Studna, A. A. Dielectric functions and optical parameters of Si, Ge, GaP, GaAs, GaSb, InP, InAs, and InSb from 1.5 to 6.0 eV. *Phys. Rev. B: Condens. Matter Mater. Phys.* **1983**, 27, 985–1009.
- (45) Johnson, P. B.; Christy, R. W. Optical constants of the noble metals. *Phys. Rev. B* **1972**, *6*, 4370–4379.
- (46) Luke, K.; Okawachi, Y.; Lamont, M. R. E.; Gaeta, A. L.; Lipson, M. Broadband mid-infrared frequency comb generation in a Si3N4 microresonator. *Opt. Lett.* **2005**, *40*, 4823–4826.